Journal of Marine Science and Application (2026) 25: 63-81
https://doi.org/10.1007/s11804-025-00698-1

RESEARCH ARTICLE

Vortex-Induced Vibration Characteristics of an Underwater Manipulator in Pulsating Flow

Yongqi Li[1], Xia Liu[2], Zongqiang Li[3], Derong Duan[1], Senliang Dai[1] and Hui Zhang[1]

Received: 30 October 2024 / Accepted: 08 April 2025

Abstract

Vortex-induced vibration (VIV) of an underwater manipulator in pulsating flow presents a notable engineering problem in precise control due to the velocity variation in the flow. This study investigates the VIV response of an underwater manipulator subjected to pulsating flow, focusing on how different postures affect the behavior of the system. The effects of pulsating parameters and manipulator arrangement on the hydrodynamic coefficient, vibration response, motion trajectory, and vortex shedding behaviors were analyzed. Results indicated that the cross-flow vibration displacement in pulsating flow increased by 32.14% compared to uniform flow, inducing a shift in the motion trajectory from a crescent shape to a sideward vase shape. In the absence of interference between the upper and lower arms, the lift coefficient of the manipulator substantially increased with rising pulsating frequency, reaching a maximum increment of 67.0%. This increase in the lift coefficient led to a 67.05% rise in the vibration frequency of the manipulator in the in-line direction. As the pulsating amplitude increased, the drag coefficient of the underwater manipulator rose by 36.79%, but the vibration frequency in the cross-flow direction decreased by 56.26%. Additionally, when the upper and lower arms remained in a state of mutual interference, the cross-flow vibration amplitudes of the upper and lower arms were approximately 1.84 and 4.82 times higher in a circular–elliptical arrangement compared to an elliptical–circular arrangement, respectively. Consequently, the flow field shifted from a P+S pattern to a disordered pattern, disrupting the regularity of the motion trajectory.

Keywords Underwater manipulator; Pulsating flow; Vortex-induced vibration; Trajectory; Overlapping mesh method

1 Introduction

Marine engineering equipment, such as underwater manipulators, offshore platforms, and offshore risers, will play a key role in the exploitation of marine resources (Min et al., 2023; Silva-Ortega et al., 2017). When steady flow passes over a cylindrical structure, vortex shedding occurs periodically behind. The alternating shedding of vortices forms in-line (IL) and cross-flow (CF) forces. The alternating effects of lift and drag contribute to the instability of the structure and produce vibration (Sharma et al., 2022). This interaction between the fluid and the structure, driven by periodic vortex shedding, is called vortex-induced vibration (VIV). Numerous scholars have extensively studied VIV in marine equipment, revealing that its cross-sectional shape, layout, and flow-field state notably influence its vibration characteristics (Williamson and Govardhan, 2008; Shahzer et al., 2022; Tu et al., 2015). However, changes in ocean flow conditions can be attributed to the influence of waves, and VIV behavior in pulsating flow notably differs from that in uniform flow. Variations in pulsation frequency and amplitude result in transverse VIV that exhibits intermittent and hysteretic characteristics.

Bluff body VIV has attracted considerable scholarly attention domestically and internationally, resulting in a substantial amount of research findings. The vibration response of single and elliptical cylinders has been comprehensively investigated in existing VIV research (Williamson and Govardhan, 2004; Raghavan and Bernitsas, 2008). Jauvtis and Williamson (2004) conducted 2-DOF VIV experiments on cylindrical structures and concluded that, for mass ratios less than 6.0, IL vibration had a substantial impact on CF vibration. Kang and Jia (2013) explored how different CF, IL natural vibration frequencies, and reduced velocities (U_r) contributed to the generation of various forms in cylinder VIV trajectory. Nguyen and Nguyen (2016) further ana-

Article Highlights

- The effect of pulsating flow on the vortex-induced vibration of an underwater manipulator is determined.
- The motion trajectory is modulated in pulsating flow.
- The flow-field pattern is strongly affected by the posture of the manipulator.
- As the pulsation amplitude increased from 0.2 to 0.4, the cross-flow amplitude decreased by 53.85%.

✉ Derong Duan
me_duandr@ujn.edu.cn

[1] School of Mechanical Engineering, University of Jinan, Jinan 250022, China

[2] Shandong Taikai Transformer Co. Ltd, Taian 271025, China

[3] JIER Machine-tool Group Co. Ltd, Jinan 250011, China

lyzed the VIV trajectories and found that the typical figure-of-eight trajectory shape was clearly observed at low U_r and collapsed into crescent or stick shapes at higher U_r. Chen et al. (2020) investigated the VIV phenomenon at moderate Reynolds numbers (ranging from 1 155 to 6 934) and observed a 2S vortex shedding pattern when the cylinder vibrated slightly. For flow around an elliptical cylinder, the difference between the long and short axes increased the complexity of the fluid force. In addition, the vibration response amplitude of the elliptical cylinder increased with the aspect ratio (AR) (Zhao et al., 2019). Kumar et al. (2018) found that when the AR = 0.5, the cylinder displayed minimal vibration amplitudes of practical importance, making the AR = 0.5 cylinder a stable or least susceptible shape to VIV. Additionally, the streamlined profile of the elliptical cylinder delayed vortex shedding and reduced the average vortex volume intensity (Wang et al., 2022). Previous studies have extensively analyzed the VIV of cylinders from the aspects of mass ratio, U_r, and AR.

The tandem arrangement is a commonly used configuration in marine engineering structures. The VIV of double cylinders exhibits different vibration characteristics due to the interaction between cylinders. Bao et al. (2012) investigated the VIV of cylinders with different spacings and found that the vibration characteristics of the upstream cylinder resembled those of a single cylinder when the center distance of the cylinder was 5.0*D*. The gap vortices around the bottom surface of the upstream cylinder exerted positive work on the downstream cylinder, which helped sustain the vibration of the upstream cylinder (Qin et al., 2019). The response of the downstream cylinder depended on the velocity of the upstream cylinder, with its own velocity determined by the actual mean wake velocity. Moreover, when the upstream cylinder was elliptical, an increase in AR led to reductions in the distance between the two cylinders and the wake turbulence intensity (Cheng et al., 2022). Fu et al. (2018) considered the VIV response of tandem cylinders with different spacing ratios under an $Re = 100$ using numerical calculations. Their research showed that the lift and drag coefficients of the downstream cylinder demonstrated a “jump phenomenon” near $U_r = 7.2$. As a common flow type in the ocean, the VIV response characteristics in shear flow are also complex. Dai et al. (2025) examined the VIV vibration characteristics of an underwater manipulator under shear flow using a self-built VIV test bench. The results showed that as U_r increased, the dimensionless amplitude increased rapidly in the IL, with a maximum value of 0.13*D*. Gao et al. (2019) analyzed the VIV of a riser under uniform and shear flow conditions, observing the multifrequency vibration characteristics of the structure. Overall, the shape and spacing of the upstream and downstream cylinders lead to different vibration responses. Additionally, the vibration characteristics of cylindrical VIV are affected by the flow field.

The above studies demonstrate that VIV can lead to fatigue damage in marine structures such as underwater manipulators. Currently, most research mainly focuses on analyzing the VIV of cylindrical structures in uniform flow fields. However, the pulsating flow generated by ocean waves can substantially affect the VIV response. Under the influence of pulsating flow, underwater manipulators with large AR exhibit highly complex VIV responses. Considerable differences are found in the VIV behavior between pulsating and steady flows. (Neshamar and O’Donoghue, 2022; Fu et al., 2014). In pulsating flow, CF vibrations are characterized by intermittent VIV, amplitude modulation, hysteresis, and build-up-lock-down cycles (Fu et al., 2018; Deng et al., 2021). In addition, Muddada et al. (2021) observed that for larger pulsating amplitudes, the wake length became shorter and wider, bringing it closer to the vortex formation. Zhao and Cheng (2014) conducted a numerical simulation of flow around two tandem circular cylinders in pulsating flow, revealing the vortex shedding patterns for circular cylinders with different gap ratios. Dorogi et al. (2023) investigated the vibration response of a two-dimensional circular cylinder under single-degree-of-freedom vibration constraints under oscillating flow. Their results showed that the cylinder experienced amplitude modulation and hysteresis, exhibiting intermittent vortex-induced vibration during the oscillation period. This study illustrated the complex hydrodynamics of transient VIV and its influence on modeling theory, particularly in unsteady flow conditions.

The VIV response of ocean engineering structures in pulsating flow is substantially affected by the cross-sectional shape, arrangement, and flow field. In the case of underwater manipulators, factors such as changes in cross-sectional shape and arm arrangement during operation can affect the hydrodynamic coefficients, vortex shedding, vibration frequency, and vibration trajectory. Therefore, this study considers the pulsating flow parameters in Bohai Bay, China, and uses numerical calculations to analyze the vibration response of an underwater manipulator under different pulsation parameters and manipulator arrangements. The effects of different pulsation frequencies and amplitudes on the manipulator’s vibration response in different postures were investigated. The results provide a theoretical basis for studying the VIV response characteristics of marine engineering equipment, which will be valuable for the further exploration and utilization of marine resources.

2 Model building

2.1 Mathematical model

Aiming to facilitate the simulation-based analysis performed in this study, a simplified model of the underwater manipulator was established, as shown in Figure 1. The three-dimensional flow field becomes stable and closely resembles a two-dimensional flow field as the fluid flows across the underwater manipulator, moving away from the free end. Therefore, this study focuses on the two-dimensional cross-sections at the midpoint of arm 2, analyzing the influence of the cross-sectional shape and arrangement on the VIV of the underwater manipulator. Arm 1 was maintained in a vertical direction, while arm 2 rotated within a range of rotation angles β from 0° to 360°. The manipulator rotated clockwise in the positive direction. When arm 2 rotated between 90° and 270°, no mutual interference was found between arm 1 and 2. The cross-section at the midpoint of arm 2 was selected to investigate the VIV response characteristics of the underwater manipulator at four typical β values: 45°, 135°, 180°, and 315°, with the corresponding manipulator postures labeled as A1, A2, A3, and A4, respectively.

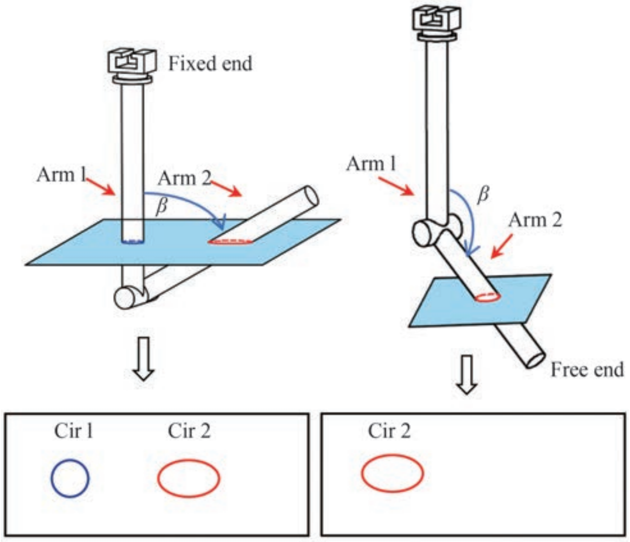

(a) Underwater manipulator in a state of interaction (b) Underwater manipulator in a state of non-interference

Figure 1 Flow field of dual-arm underwater manipulator

Table 1 presents the posture model of the underwater manipulator for four typical β values. The blue and red cylinders represent arms 1 and 2, respectively. The length of the upper arm L_1 is 400 mm, while that of the lower arm L_2 is 320 mm. For A1, when arm 2 is rotated by 45°, the downstream arm 2 experiences substantial and unstable fluid forces as the incoming flow passes through the manipulator, owing to the influence of the upstream arm 1. In addition, considering a spacing ratio $L/D = 4.24$ (where L and D are the manipulator center distance and diameter, respectively), the downstream arm 2 also exerts some impact on the upstream arm 1 (Dalton et al., 2001). However, when arm 2 is rotated by 135° and 180° (i.e., for A2 and A3, respectively), no notable mutual interference occurred between arms 1 and 2. In A4 ($\beta = 315°$), arms 1 and 2 were in a state of mutual interference. Compared to A1 postures, the cross-section of the upstream arm 2 is elliptical in this case, resulting in a different flow field.

2.2 Governing equations

The vortex-induced flow field around the underwater manipulator is an unsteady, incompressible, two-dimensional turbulent flow field. Therefore, the two-dimensional unsteady Reynolds Averaged Navier–Stokes (URANS) method is employed in this study to solve the flow field (Kim et al., 2021), as described below.

$$\frac{\partial U_i}{\partial x_i} = 0 \tag{1}$$

$$\frac{\partial U}{\partial t} + U_j \frac{\partial U_i}{\partial x_j} = -\frac{1}{\rho}\frac{\partial P}{\partial x_i} + v\frac{\partial^2 U_i}{\partial x_j^2} - \frac{\partial \overline{u_i u_j}}{\partial x_j} \tag{2}$$

where ρ denotes fluid density, t denotes time, U_i and U_j are the velocity vectors, x_i and x_j are the position vectors of the fluid unit, and P is the pressure. $\overline{u_i u_j}$ is the Reynolds stress tensor (Tennekes and Lumley, 1972).

$$\overline{u_i' u_j'} = \mu_t\left(\frac{\partial U_i}{\partial x_j} + \frac{\partial U_j}{\partial x_i}\right) - \frac{2}{3}\delta_{ij}k \tag{3}$$

where k is turbulent kinetic energy, μ_t denotes turbulent viscosity, and δ_{ij} is the Kronecker sign.

The SST $k-\omega$ turbulence model is particularly suitable for capturing the characteristics of plane shear layers and flow separation at the rear of bodies, making it effective for accurately representing various aspects of turbulence flow. In addition, this model has been extensively validated and widely applied in similar studies. Thus, the SST $k-\omega$ turbulence model is adopted in the present work to model the Reynolds stress tensor (Yu et al., 2020). The governing equations for this turbulence model comprise the k equation and the ω equation.

$$\frac{\partial(\rho k)}{\partial t} + \frac{\partial(\rho k U_i)}{\partial x_i} = \frac{\partial\left(\Gamma_k \frac{\partial k}{\partial x_j}\right)}{\partial x_j} + G_k - Y_k + S_k \tag{4}$$

$$\frac{\partial(\rho\omega)}{\partial t} + \frac{\partial(\rho\omega U_i)}{\partial x_i} = \frac{\partial\left(\Gamma_\omega \frac{\partial \omega}{\partial x_j}\right)}{\partial x_j} + G_\omega - Y_\omega + D_\omega + S_\omega \tag{5}$$

where G_ω denotes the ω equation. Γ_k and Γ_ω represent the effective diffusion terms of k and ω, respectively. Y_k and Y_ω represent the divergence of k and ω, respectively. D_ω represents the orthogonal divergence term. S_k and S_ω are user-defined.

The 2-DOF structural control equation of this elastically mounted structure can be described as follows:

Table 1 Calculation model of the manipulator under different rotation angles

Attitude	Rotation angle β of arm 2	Mathematical model	Computational model
A1	45°	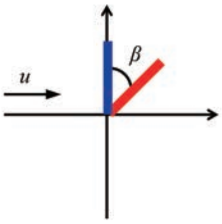	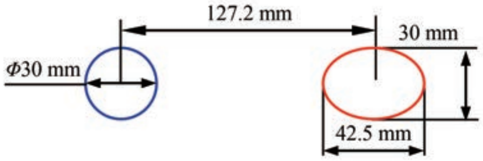
A2	135°	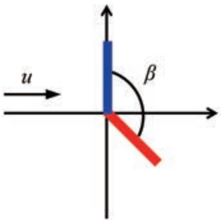	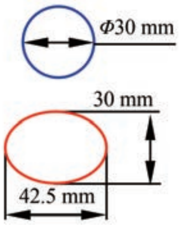
A3	180°	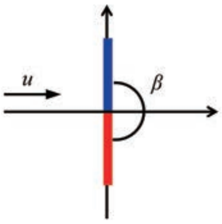	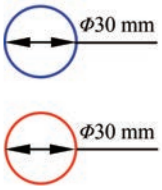
A4	315°	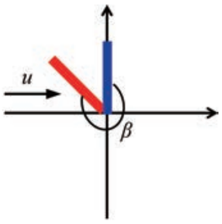	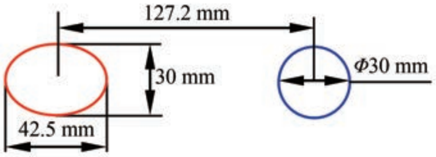

$$m\frac{\partial^2 x}{\partial t^2} + 2m\omega_0\zeta\frac{\partial x}{\partial t} + m\omega_0^2 x = f_D(t) \tag{6}$$

$$m\frac{\partial^2 y}{\partial t^2} + 2m\omega_0\zeta\frac{\partial y}{\partial t} + m\omega_0^2 y = f_L(t) \tag{7}$$

where ζ is the damping ratio. Meanwhile, $\partial^2 x/\partial t^2$, $\partial x/\partial t$, and x represent the in-line acceleration, velocity, and displacement of the cylinder, respectively. $\partial^2 y/\partial t^2$, $\partial y/\partial t$, and y represent the same quantities associated with the cross-flow motion, ω_0 is the natural circular frequency, c is the damping coefficient, and $f_D(t)$ and $f_L(t)$ are the fluctuating drag and lift forces acting on the structure surface, respectively. The selected damping ratio ζ in this work is 0.00542.

2.3 Boundary conditions and parameters setting

In this study, the two-dimensional underwater manipulator was simplified as a mass–spring–damping system. A spring–damping unit was employed to calculate the manipulator stiffness, allowing it to vibrate freely in the IL and CF directions (corresponding to the x and y directions, respectively). Figure 2 illustrates the fluid domain and the associated boundary conditions.

Herein, D was 0.03 m, and the calculated flow-field area was $20D \times 34D$, with the origin located at the center of the manipulator. Aiming to model the pulsating flow and capture the change of wake vortices, the distances from the origin to the upstream and downstream entrances were set to $10D$ and $24D$, respectively. The distance between the sides was $10D$. A velocity inlet condition was applied to the inlet, while a pressure outlet condition was applied to the domain exit. No-ship boundary conditions were applied to the side walls.

Based on the average velocity in the Bohai Sea and Yellow Sea, this study was conducted under a mean velocity condition of $u_m = 0.2$ m/s. Therefore, the Reynolds number was calculated as $Re = 6000$ using the following expression:

$$Re = \frac{\rho u_m D}{\mu} \tag{8}$$

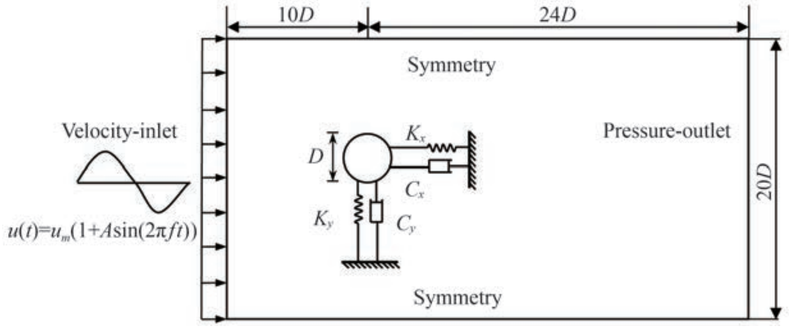

Figure 2 Fluid domain and boundary condition

where μ is the hydrodynamic viscosity.

The fluid flow is unstable due to the influence of ocean waves. In this study, this unstable incoming flow was simplified as a sinusoidal pulsation variation. The effects of the sinusoidal pulsation frequency f and the pulsation amplitude A (dimensionless) on the vibration were then examined. The pulsating incoming flow was modeled as follows:

$$u(t) = u_m\left[1 + A\sin\left(2\pi ft\right)\right] \tag{9}$$

where $u(t)$ is the inlet pulsation velocity, t is time, and u_m is the uniform flow velocity. The pulsating flow velocity varied with A and f. The values of A and f were then determined based on the wave conditions in ocean flow. Table 2 presents seven groups of different pulsation conditions.

Table 2 Fluid parameter of pulsating flow

Parameters	A	f (Hz)
Case 1	0	0
Case 2	0.2	0.2
Case 3	0.2	0.3
Case 4	0.2	0.4
Case 5	0.3	0.2
Case 6	0.4	0.2
Case 7	0.4	0.4

An overlapping mesh is highly suitable for dynamic simulations because it facilitates unconstrained relative displacements between individual mesh regions. In addition, after the generation of the overlapping mesh, no further modification is required, ensuring high mesh quality throughout the simulation. Therefore, in this study, overlapping mesh techniques were employed by generating a foreground mesh for the cylindrical components and a separate background mesh for the surrounding flow domain. Data within the overlapping part was interpolated to realize data transmission. The flow field calculation model is shown in Figure 3, where the foreground and background grids were structured grids.

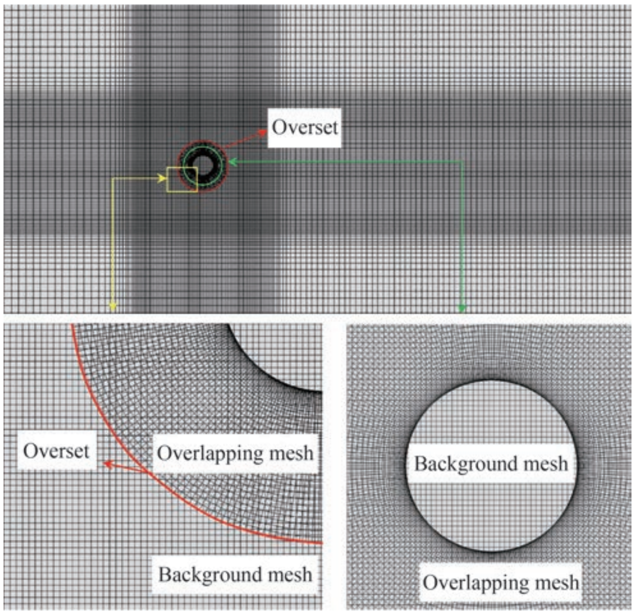

Figure 3 Employed mesh system and zoom-in-view of the mesh close to the structure surface

2.4 Grid independence and time step verification

A mesh independence test was conducted to ensure that the calculation results were independent of the number of grids. This test demonstrated that the mesh configuration used in this study had a negligible effect on the numerical outcomes. Table 3 shows the results of the grid independence verification, revealing the average drag coefficients (C_D) and the root mean square of the lift coefficients ($C_{L,\,\mathrm{rms}}$) obtained from the three sets of meshes. As the mesh was refined from Mesh 1 to Mesh 2, the RMS error of the lift coefficient was 0.637%, and the average error in the drag coefficient was 2.015%. Further refinement from Mesh 2 to Mesh 3 resulted in an RMS error of 0.478% for the lift coefficients and an average error of only 0.036% for the drag coefficient. These results indicate the differences between the two results were minimal. Thus, Mesh 2 was selected for subsequent simulations, balancing accuracy with calculation efficiency.

Table 3 Calculation results under different grid numbers

Mesh	Nodes of background	Nodes of foreground	C_D	$C_{L,\mathrm{rms}}$
M1	22512	2200	1.262	0.8179
M2	32224	2400	1.260	0.8341
M3	42781	2900	1.254	0.8344

The selection of the time step is crucial in the process of transient solver flow-around calculations. In this study, the following three time steps were selected: 0.01, 0.02, and 0.03 s. Under the same Reynolds number and other conditions, the VIV of the manipulator in vertical postures was calculated. The lift and drag coefficients were also used to assess the influence of different time steps on the simulation results.

The lift and drag coefficient data for different time steps were compared, as presented in Table 4. Notably, reducing the time step from 0.02 to 0.01 s resulted in a decrease in the errors of the lift and drag coefficients by 1.61% and 0.36%, respectively. When the time step was increased to 0.03 s, the relative errors in the lift and drag coefficients were 2.14% and 2.88%, respectively. Therefore, considering calculation accuracy and efficiency, a dimensionless time step of 0.02 s was selected.

Table 4 Calculation results at different time steps

Time steps (s)	C_D	$C_{L,\mathrm{rms}}$
0.03	1.287	0.858
0.02	1.260	0.834
0.01	1.240	0.831

2.5 Accuracy verification of numerical method

Aiming to verify the accuracy of the SST $k-\omega$ turbulence model, the amplitude of the VIV responses in the CF of the cylinder at different U_r was compared with the classical experimental results of Khalak and Williamson (1996), as well as the numerical simulation results of Xu et al. (2022) and Zheng and Wang (2017). These comparisons are shown in Figure 4, where the detailed parameters of the cylinder are introduced. The dimensionless fluid velocity U_r is expressed as follows:

$$U_r = \frac{u_m}{f_n D} \tag{10}$$

where f_n is the natural frequency of the structure.

Under the condition of $U_r = 5$, the simulation results in this study differ by 7.0% from the reference results. In addition, the maximum error in the mean values was 5.71%. This difference can be attributed to variations in vibration frequency related to different numerical or experimental conditions, as well as differences in the Reynolds number. Therefore, these comparison results verify the accuracy of the numerical method used in this study.

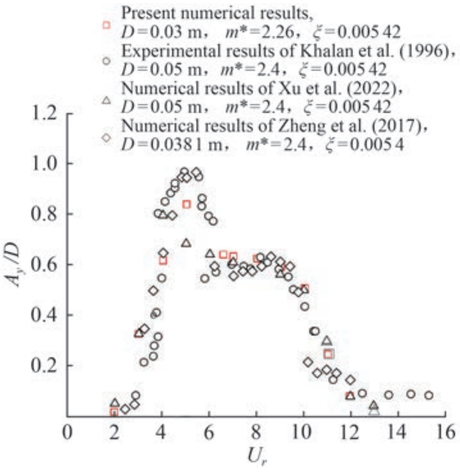

Figure 4 VIV vibration amplitudes of the structure displacement in the CF direction

3 Results and discussion

3.1 The influence of incoming flow form on the response characteristics of underwater manipulator

The VIV response characteristics were analyzed under uniform and pulsating flows (Cases 1 and 2, respectively) to explore the influence of pulsating flow on the manipulator. The A2 and A3 postures of the manipulator, as listed in Table 1, were selected for this analysis. The time history curves of the lift and drag coefficients of the manipulator under the two different inflow conditions are illustrated in Figure 5. When the rotation angle was 135°, the lift coefficient exhibited a strong regularity under uniform flow, with its waveform closely resembling a standard sine form. Under pulsating flow conditions, the lift coefficient continued to fluctuate sinusoidally over time. However, multiple extreme values appeared within each cycle. Additionally, the maximum lift coefficient under pulsating flow reached 0.164, which was approximately 1.84 times higher than under uniform flow. The drag coefficient remained relatively stable under uniform flow but exhibited a substantial increase under pulsating flow. The drag coefficient in pulsating flow was approximately 1.46 times higher than that under uniform flow. The nonstationary fluctuations of the drag coefficient can be attributed to the varying intensity of the pulsating flow and the variable impact positions on the surface of the manipulator (Gupta et al., 2020).

When β reached 180°, the $C_{L,\max}$ and $C_{D,\max}$ increased by

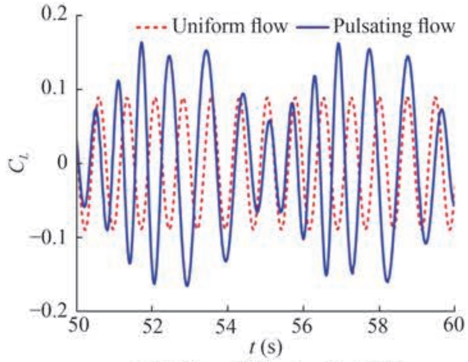

(a) Lift coefficients, $\beta=135°$

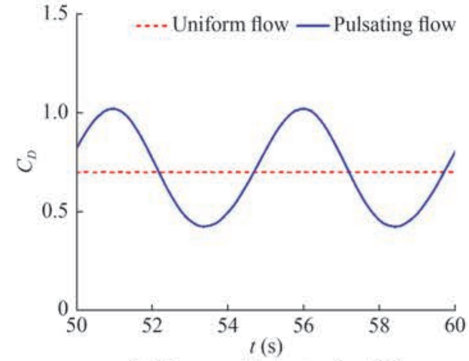

(b) Drag coefficients, $\beta=135°$

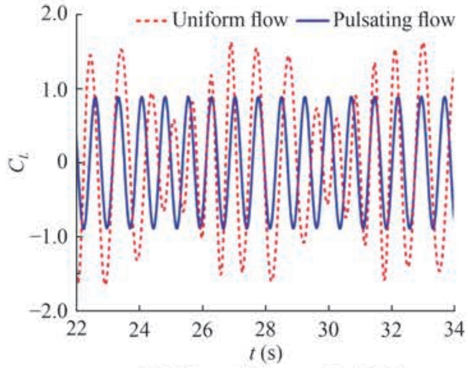

(c) Lift coefficients, $\beta=180°$

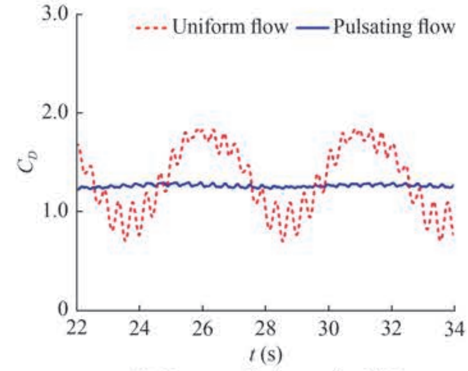

(d) Drag coefficients, $\beta=180°$

Figure 5 Time history curve of the lift and drag coefficients

53.98% and 42.97%, respectively, compared to uniform flow. In other words, the superimposed pulsating flow increased the force on arm 2, with the effect being more pronounced when the cross-section axial ratio was smaller.

A major cause of vibration in the CF direction of the manipulator is vortex shedding (Liu et al., 2020). In steady flow, the vortex-shedding frequency is equal to the lift frequency for vortex-induced cylindrical vibrations. Aiming to further investigate the effect of pulsating flow on arm 2, the fast Fourier transform of the lift curve and structural displacement response were performed to determine the vortex-shedding and structural vibration frequencies, respectively. Figure 6 shows the spectral analysis results obtained for the displacements and C_L of the underwater manipulator's VIV system under uniform and pulsating flows. When the incoming flow was uniform flow, the CF amplitude of the elliptical cross-section was 1.783×10^{-3}, which was considerably smaller than that of the circular cross-section. After the pulsating flow was introduced, the CF amplitude of the circular cross-section was approximately 73 times larger than that of the elliptical cross-section. The amplitude comparison between the IL and CF directions under uniform flow in Figure 6(a) revealed that the CF amplitude was approximately 21.7 times greater than that of the IL. As shown in Figure 6(b), the CF amplitude was approximately 5.3 times the IL amplitude. In other words, the CF amplitude was approximately one order of magnitude greater than the IL direction amplitude (Bao et al., 2012; Liu et al., 2020). The multifrequency phenomenon observed under pulsing inflow is a typical characteristic of the oscillatory flow response (Mittal, 2017), with the corresponding amplitude being smaller than that under uniform flow.

The trajectory shape plays a crucial role in determining the amplitude and frequency content of fluid dynamics, which is closely related to the energy transfer between the fluid and the structure (Kozakiewicz et al., 1997). Figures 7 and 8 show the trajectory of the underwater manipulator under uniform and pulsating flow conditions, respectively. Under uniform incoming flow (Figure 7), the motion trajectory was approximately crescent-shaped, which was caused by the vibration phase difference between the IL and CF directions near 90° or 270° (Bourguet et al., 2013). Additionally, the displacement in the *y*-direction was considerably higher than that in the *x*-direction. Compared with Figure 7, after the pulsating flow was applied, the displacement range of the manipulator notably increased. Specifically, as depicted in Figure 8(a), when the cross-section was elliptical, the vibration exhibited a composite pattern of multiple "∞" superpositions of different sizes. The overall trajectory resembled a lateral vase, with the displacement along the *x*-axis being larger than along the *y*-axis. This behavior can be attributed to the superposition of multiple vibration frequencies in response to the pulsating flow and the enhanced interference from the incoming flow. When the cross-section was circular, the vibration trajectory comprised multiple "8" with different sizes, which corresponds with the figure-eight trajectory shape found by Nguyen and Nguyen (2016).

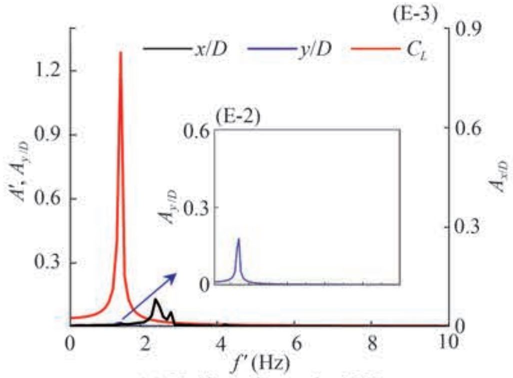

(a) Uniform flow, β=135°

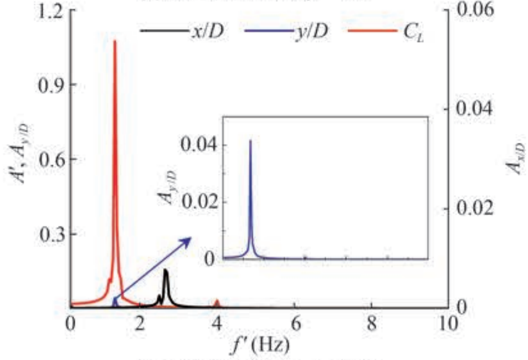

(b) Uniform flow, β=180°

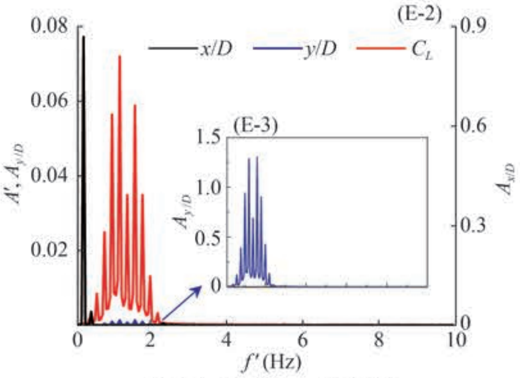

(c) Pulsating flow, β=135°

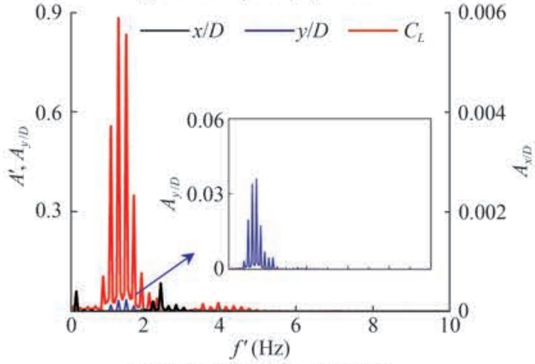

(d) Pulsating flow, β=180°

Figure 6 Spectral analysis of displacement and lift coefficient

The difference in vortex shedding behaviors also contributed to the variation in the trajectory of the manipulator under the two different incoming flows (Yun et al., 2017).

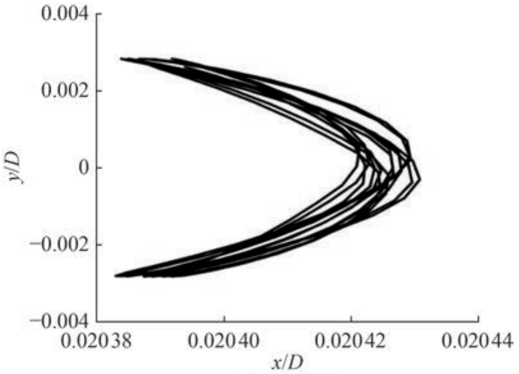

(a) β=135°

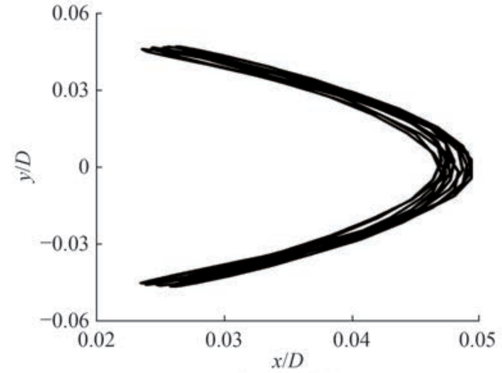

(b) β=180°

Figure 7 Trajectories of the underwater manipulator under uniform flow

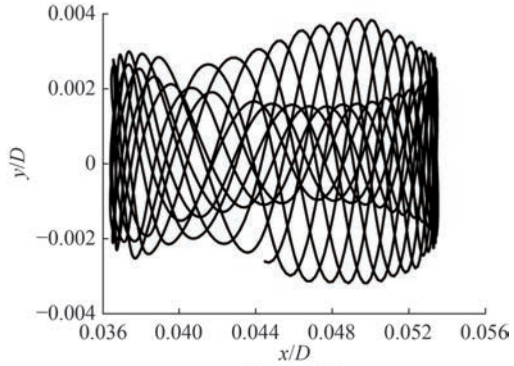

(a) β=135°

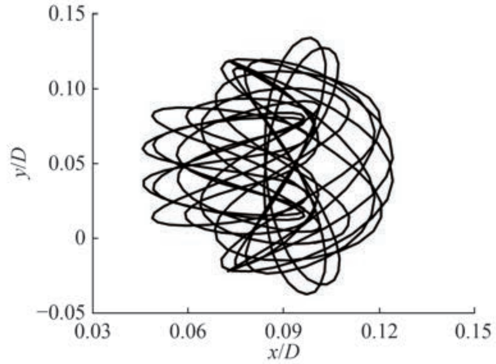

(b) β=180°

Figure 8 Trajectories of the underwater manipulator under pulsating flow

Figure 9 shows the variations in the wake-field instantaneous vorticity diagrams for different inlet flows. In the figure, the red and blue vortices represent positive and negative vorticity, respectively. Notable differences were observed in the wake patterns of underwater manipulators with different cross-section shapes. When the cross-section was elliptical, the vortex shedding pattern behaved similarly to that of a fixed elliptical cylinder due to the small transverse amplitude. By contrast, the AR of the elliptical cross-section in this study was close to 0.5, making it less susceptible to VIV (Zhu et al., 2023). The vortices on both sides of the manipulator were longer compared to those of the circular cross-section, resulting in a lower vibration degree. In addition, under uniform flow conditions, the wake distribution was relatively uniform. The vortices were shed from the upper and lower sides of the manipulator, and the wake exhibited the standard 2S mode. Additionally, by comparing Figures 9(c) and 9(d), the vibration amplitude of the underwater manipulator under pulsing flow was substantially higher than that under uniform flow. This finding indicates that the force acting on the manipulator drastically increased under pulsing flow, which is consistent with the trend observed in Figure 5.

3.2 The influence of pulsation parameters on the response characteristics of underwater manipultor

Aiming to further explore the influence of pulsating flow parameters on the VIV response of the underwater manipulator, the C_L and C_D, representing the centroid trajectory and vortex shedding of the elliptical section manipulator, respectively, under different f and A values, were analyzed.

3.2.1 Effect of pulsating frequency

The calculation results for Cases 2–4 were considered in this analysis. Figure 10 illustrates the C_L and C_D curves after the flow stabilizes. The C_L curves exhibited a clear beat form, indicating that the force coefficient amplitude had a

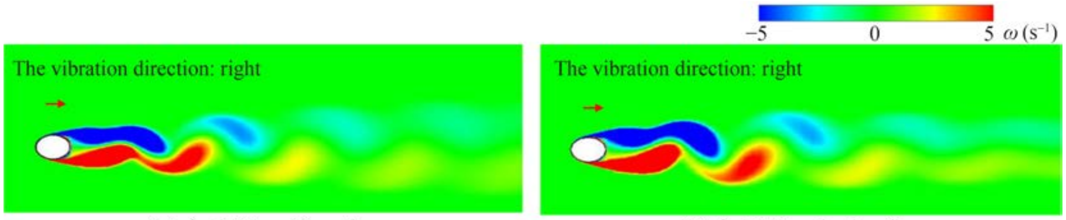

(a) β=135°, uniform flow (b) β=135°, pulsating flow

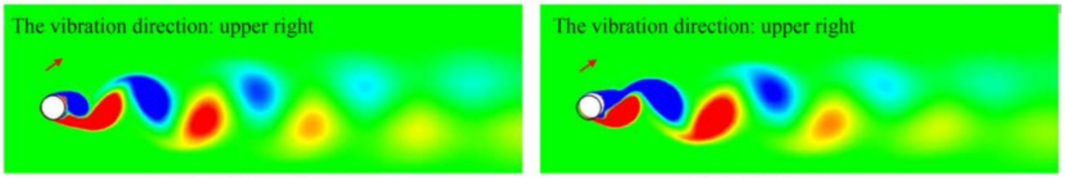

(c) β=180°, uniform flow (d) β=180°, pulsating flow

Figure 9 Flow field around manipulator with different inlet flows

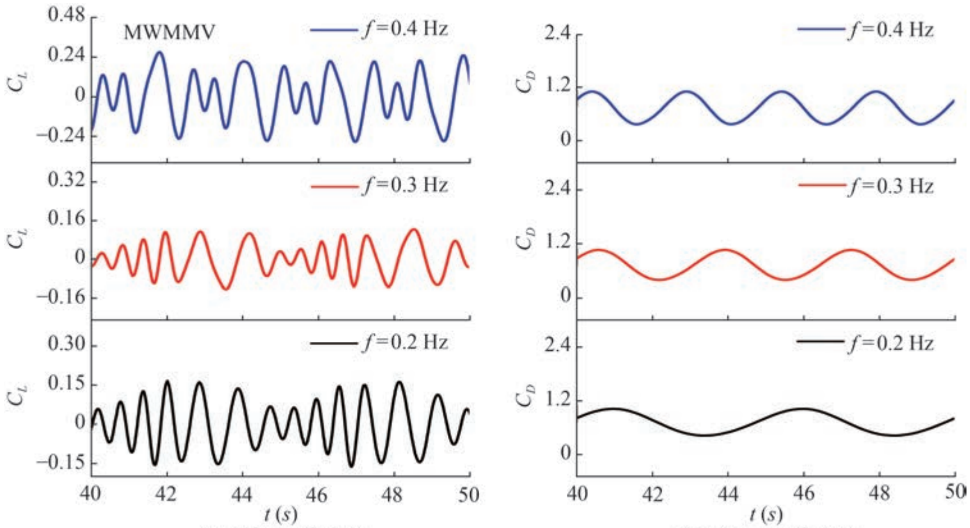

(a) Lift coefficient (b) Drag coefficient

Figure 10 Time histories of lift and drag forces acting on arm 2 certain long-period variation over time. This behavior occurred due to unsynchronized vortex frequency with the vibration frequency.

When f = 0.2 Hz, $C_{D,\max}$ = 1.02 and $C_{L,\max}$ = 0.16, which were lower than the values observed for elliptic cylinders under uniform flow (Kumar et al., 2018). As f increased, the lift and drag coefficients also increased. When f reached 0.4 Hz, the lift coefficient increased by 67%, while the drag coefficient showed a small increase of 7.3%. This difference can be attributed to the fact that the fluctuating pressure induced by vortex shedding intensified with increasing f (Duan et al., 2023).

The data were analyzed in the frequency domain using the wavelet transform method, thereby obtaining the VIV frequency and the corresponding amplitude, as well as the vortex-shedding frequency. Figure 11 shows the displacement and vortex shedding spectral analysis at different pulsating frequencies, where the effect of f on arm 2 is further investigated via comparative analysis. When f = 0.2 Hz, the vibration frequency of arm 2 in the x-direction was 0.25 Hz, with a corresponding vibration amplitude of 0.008 69. When f = 0.4 Hz, the vibration frequency and amplitude in the x-direction increased by 67.05% and 24.14%, respectively. This finding demonstrated an increasing trend in vibration frequency and corresponding amplitude in the x-direction as f increased. In addition, the vibration frequency in the CF direction was identical to the vortex-shedding frequency, indicating that the manipulator's vibration was synchronized with vortex shedding. When f = 0.2 Hz, the CF direction vibration and vortex-shedding frequencies were both 1.598 Hz, with the vibration and vortex-shedding amplitudes being 0.001 3 and 0.058 9, respectively. When f increased to 0.4 Hz,

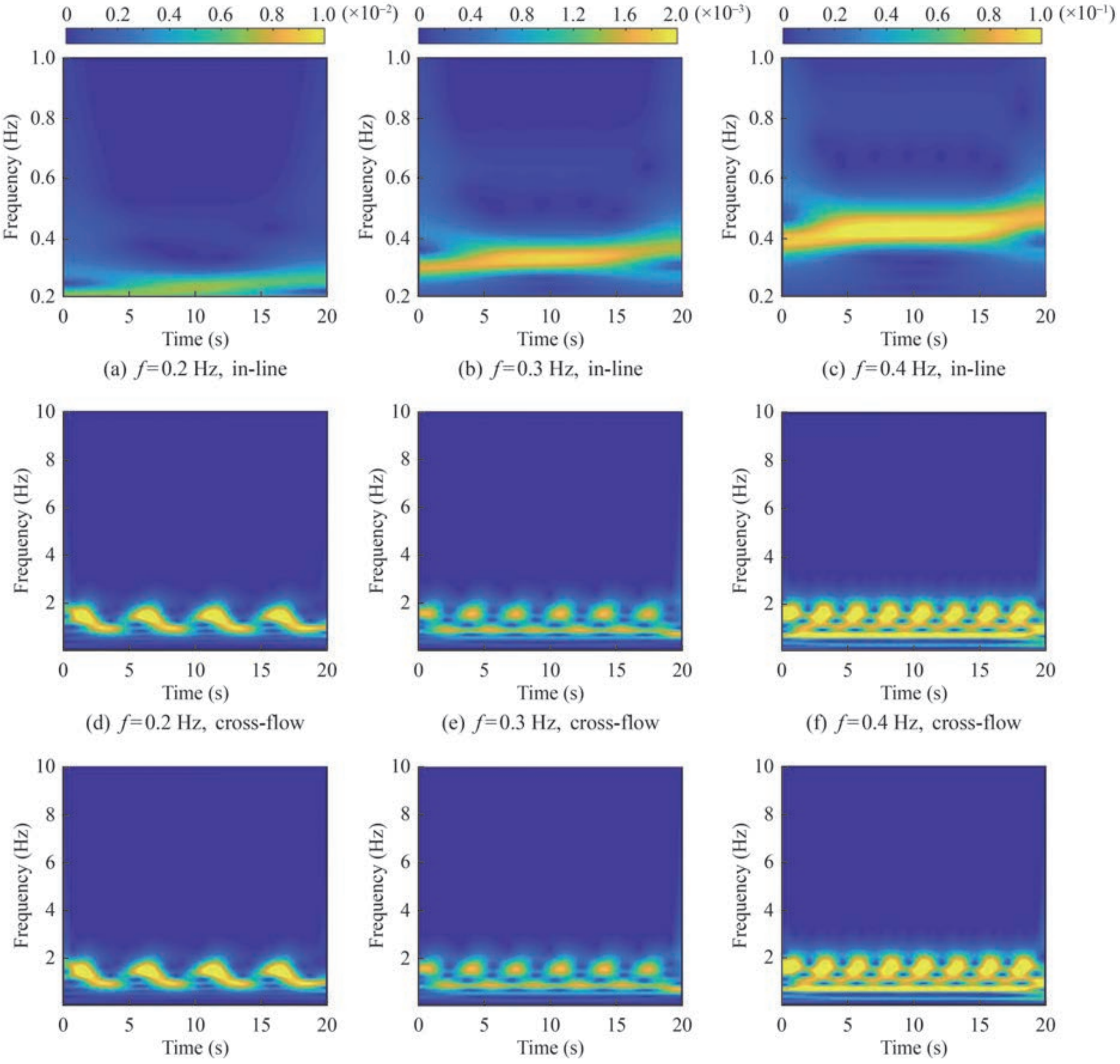

(a) f=0.2 Hz, in-line (b) f=0.3 Hz, in-line (c) f=0.4 Hz, in-line

(d) f=0.2 Hz, cross-flow (e) f=0.3 Hz, cross-flow (f) f=0.4 Hz, cross-flow

(g) f=0.2 Hz, lift coefficient (h) f=0.3 Hz, lift coefficient (i) f=0.4 Hz, lift coefficient

Figure 11 Spectral analysis of displacements and lift coefficient the CF direction vibration and vortex-shedding amplitudes increased by 69.23% and 126.32%, respectively. This finding further indicated that the oscillatory force acting on the upper and lower manipulator surfaces was enhanced as *f* increased.

Figure 12 shows the trajectory profiles obtained of the underwater manipulator obtained for different *f* values. In the range of 0.2–0.4 Hz, the VIV trajectory of the underwater manipulator showed a diversified trend. Analysis results revealed that the underwater manipulator exhibited a discernible pattern in its overall trajectory, with the displacement of arm 2 along the *x*-direction being notably larger than that along the *y*-direction. This observation aligns with the values shown in Figure 11. When f = 0.2 Hz (Figure 12(a)), the trajectory shape was similar to that of a vase placed on its side. As the CF displacement increased, the IL displacement decreased, reaching a minimum value at $x = 1.2 \times 10^{-3}$ (with a shape similar to the neck of a vase). Subsequently, the IL displacement increased as the CF displacement continued, having a maximum value at $x = 1.5 \times 10^{-3}$. When f = 0.3 Hz (Figure 12(b)), the trajectory of the manipulator resembled that of a vase with a large mouth and a small bottom. When the pulsating frequency was 0.4 Hz, the motion trajectory in the *y*-direction gradually decreased over time. This change further indicated the influence of pulsating frequency on the VIV trajectory (Silva-Ortega and Assi, 2017).

Figure 13 shows the vorticity clouds of the manipulator at three sets of pulsation frequencies, where (a), (b), and (c) correspond to f = 0.2, 0.3, and 0.4 Hz, respectively. During the vortex shedding period *T*, distinct positive and negative vortices formed at the trailing edge of the elliptical cylinder and developed downstream. The vortex generated at the lower rear of the elliptical column reached its maximum lift force at $t = t_0 + 1/3T$. Subsequently, this vortex migrated toward the rear of the elliptical column, reaching its position at $t = t_0 + 2/3T$. As time progressed, the shedding vortex gradually moved along the centerline of the elliptical cylinder, gradually moving away from the elliptical cylinder and eventually dissipating its energy. At $t = t_0 + T$, another vortex was also generated at the upper rear of the elliptical column, resulting in a maximum negative lift force. Additionally, at the start time t_0, as *f* increased, the upstream vortex length decreased from 0.14 to 0.11. Moreover, secondary vortex shedding became more pronounced. Flow separation and vortex shedding were weak due to the close streamline profile of the elliptical cylinder. The wake vortex patterns of the elliptical cylinder remained similar across different *f* values, revealing a notable reduction in vortex spacing as *f* increased. Consistent with the trend depicted in Figure 11, an increase in *f* resulted in a corresponding rise in the frequency and energy of vortex shedding, as well as an amplification of the elliptical cylinder's amplitude.

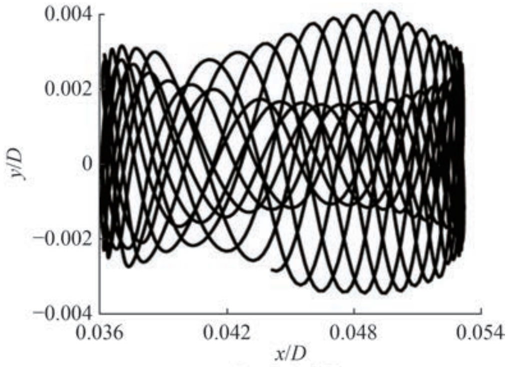

(a) f=0.2 Hz

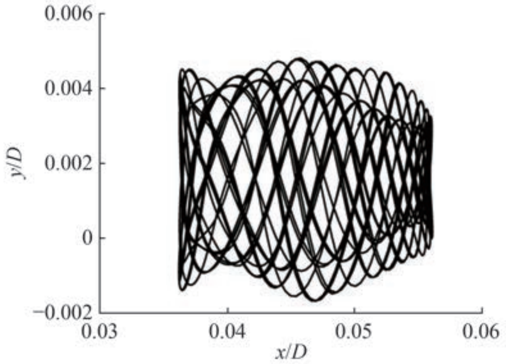

(b) f=0.3 Hz

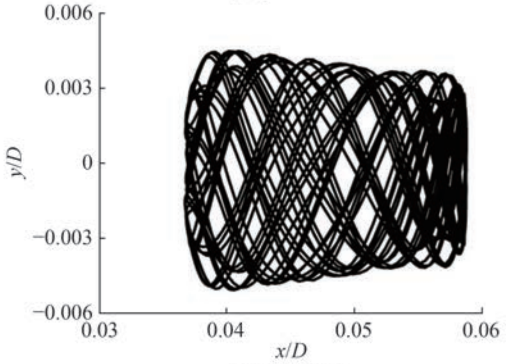

(c) f=0.4 Hz

Figure 12 Trajectories of underwater manipulator for A = 0.2

3.2.2 Effect of pulsating amplitude

In addition to pulsating frequency, the pulsating amplitude also substantially impacted the VIV response of the underwater manipulator. Therefore, this section presents an analysis of the manipulator VIV's response characteristics for different *A*, including hydrodynamic coefficients, vibration frequency, and motion trajectories. Figure 14 illustrates the C_L and C_D curves for three sets of *A* values. Notably, as the pulse amplitude increased, the lift coefficient of the manipulator exhibited a similar fluctuation trend, although with a gradual decrease in its peak value. The drag coefficient exhibited a smooth sinusoidal pattern, in which the amplitude increased with the pulse amplitude. When *A* was 0.2, $C_{L,\max}$ = 0.164; when *A* increased from 0.2 to 0.4, $C_{L,\max}$ decreased to 0.11. This outcome slightly differed

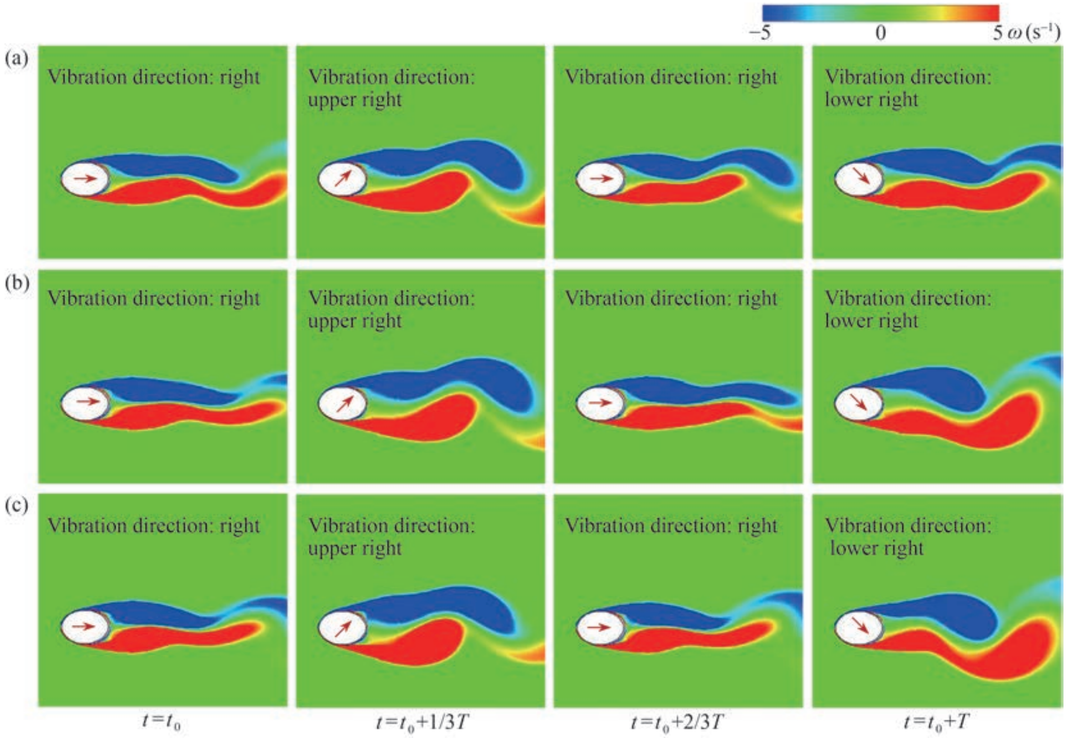

Figure 13 Formation, development, and shedding of vortices in a period

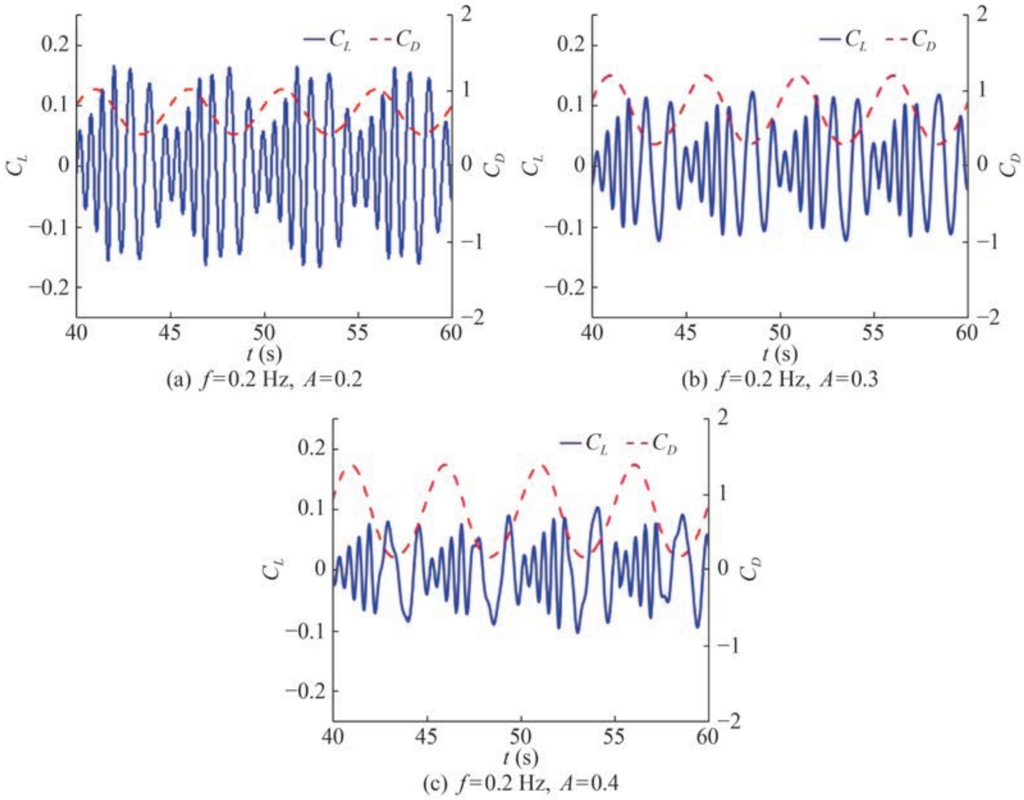

(a) f=0.2 Hz, A=0.2

(b) f=0.2 Hz, A=0.3

(c) f=0.2 Hz, A=0.4

Figure 14 Time history curve of the lift and drag coefficients

from the behavior obtained for a fixed cylinder (Zierenberg et al., 2006). For C_D, an opposite trend was observed, with $C_{D,\max}$ increasing by 36.79% as A increased. This finding showed that, as A increased, the flow field pulsation intensified, leading to a rise in the drag force on arm 2. Consequently, the sustained impact on arm 2 also increased. However, the sustained impact force from the incoming flow had no direct effect on C_L.

Table 5 lists the vibration frequency of the manipulator in the *x*-direction (f_x/D), the vibration frequency in the *y*-direction (f_y/D), the vortex shedding frequency (f_s), and the corresponding amplitudes for varying *A*. As *A* increased, the vibration frequency of arm 2 in the *x*-direction remained constant at 0.248 9. However, the vibration amplitude experienced a notable increase, rising from 0.087 to 0.017 8, representing a remarkable growth of 104.6%. As shown in Table 5, the vibration frequency in the *y*-direction, the vortex-shedding frequency, and their corresponding amplitudes all demonstrated a decreasing trend as *A* increased. Specifically, as *A* increased from 0.2 to 0.4, the *y*-direction vibration and the vortex-shedding frequencies decreased from 1.598 to 0.699 Hz, revealing a reduction of 56.26%. The corresponding amplitudes were reduced by 53.85% and 28.53%. This finding can be attributed to the influence of C_D and C_L on IL and CF displacements, respectively. This result aligns with the variations in the lift and drag coefficients exhibited in Figure14.

Table 5 Values of vibration and vortex shedding frequencies

Parameters	$f_{x/D}$	$A_{x/D}$	$f_{y/D}$	$A_{y/D}$	f_s	A'
$A = 0.2$	0.249 8	0.008 7	1.598	0.001 3	1.598	0.058 9
$A = 0.3$	0.249 8	0.013 2	0.949	0.000 9	0.949	0.052 6
$A = 0.4$	0.249 8	0.017 8	0.699	0.000 6	0.699	0.042 1

Figure 15 illustrates the underwater manipulator trajectories obtained for $f = 0.2$ Hz and $A = 0.2$, 0.3, and 0.4. Compared to the trajectories in Figure 12, the motion trajectory of the manipulator became more complex, implying that variations in pulsating amplitude exert a more substantial influence on the force exerted on the manipulator. The trajectories for all three sets of working conditions exhibited similar trends, resembling a vase placed on its side. When $A = 0.2$, arm 2 moved back and forth in the *x*-direction within a range of 0.036 to 0.053, and in the *y*-direction, arm 2 vibrated between −0.003 5 and 0.003 5. When $A = 0.4$, the displacements of arm 2 in the IL and CF directions were 0.035 and 0.005 2, respectively. As A increased, the displacement range of the underwater manipulator in the *y*-direction gradually decreased, while the displacement range in the *x*-direction increased. This displacement variation trend corresponded exactly to the C_L and C_D variation trends, as shown in Figure 14.

Figure 16 demonstrates changes in the vorticity of arm 2 within a single period under different *A* values. The vortex shedding pattern was similar to that in Figure 14, remaining in the 2S mode. As indicated in Table 4, the vibration amplitude of the elliptical cylinder was negligible, resulting in a constant flow field around the elliptical cylinder. However, as *A* increased from 0.2 to 0.4, the wake width increased by 20%. Additionally, the distance between the center of the first vortex and the elliptical cylinder decreased, while the vibration amplitude of the manipulator increased. This change was associated with the thinning of the laminar shear layer as *A* increased, which intensified the strength of the formed vortices.

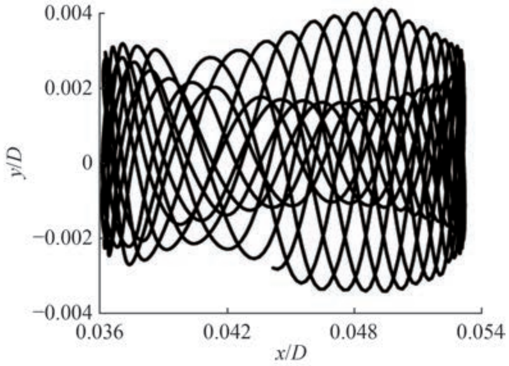

(a) f=0.2 Hz, A=0.2

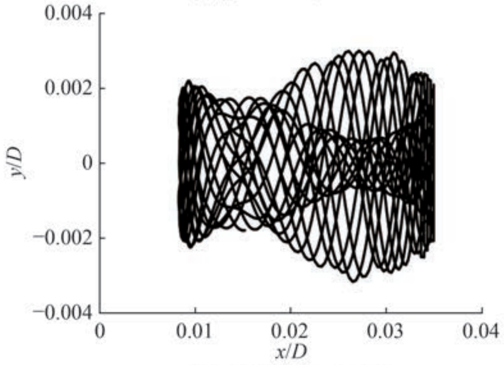

(b) f=0.2 Hz, A=0.3

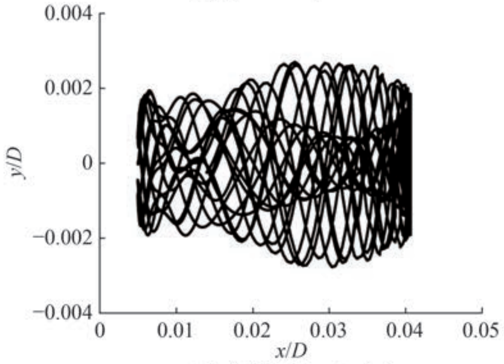

(c) f=0.2 Hz, A=0.4

Figure 15 Trajectories of the underwater manipulator under different amplitudes

3.3 The influence of arrangement form on the response of characteristics of underwater manipulator

Different postures of the manipulator alter the shape of the upstream and downstream cross-sections, which, in turn, affects the VIV response characteristics, including the force coefficients acting on the upstream and downstream arm

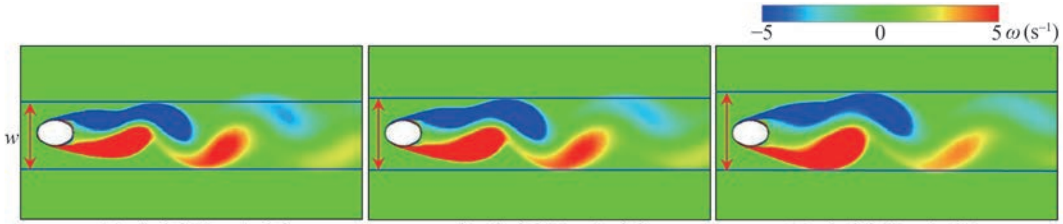

(a) f=0.2 Hz, A=0.2 (b) f=0.2 Hz, A=0.3 (c) f=0.2 Hz, A=0.4

Figure 16 Vorticity cloud maps with different pulsating amplitudes

surfaces. Herein, the VIV response analysis was performed for postures A1 and A4 under the pulsating flow condition of Case 7. Figures 17(a) and (b) show the C_L and C_D time histories at β = 45°, respectively. The solid and dotted lines represent the upstream and downstream arm coefficients, respectively. The figure clearly demonstrates that the lift and drag coefficients of the manipulator exhibited multiple peaks within the same period, indicating a heightened pulsation in the flow field. Additionally, the curve exhibited noticeable nonsmoothness. Specifically, the drag coefficient of the upstream manipulator exhibited minor fluctuations between its peaks and troughs, which distinctly contrasted with the smoother drag coefficient curve depicted in Figure 10. The maximum values observed were C_{L1} = 2.185, C_{D1} = 2.526, C_{L2} = 4.350, and C_{D2} = 1.618, where the subscripts 1 and 2 represent arms 1 and 2, respectively. The amplitude of C_{L1} was smaller than that of the downstream arm, while the amplitude of C_{D1} was larger. This finding indicates that the wake from the upstream arm affected the downstream arm during VIV, weakening the CF vibration. Notably, C_{D2} was strongly negative, indicating that the downstream manipulator was propelled forward due to this phenomenon (Raman et al., 2013). Simultaneously, the incoming flow was pulsating, increasing the impact on the upstream arm. Thus, the force exerted on the downstream arm was suppressed due to the wake from the upstream arm, which had a "shielding" effect on the part of the incoming flow. Therefore, the C_{L2} amplitude was small. Compared to the downstream elliptical section of the same shape in Figure 11(b), C_L and C_D were reduced by 61.52% and 9.33%, respectively. At β = 315°, as shown in Figures 18(a) and (b), the fluctuations in C_{L1} and C_{D1} were smaller than those observed at β = 45°. This phenomenon was due to the reduced width of the shear layer

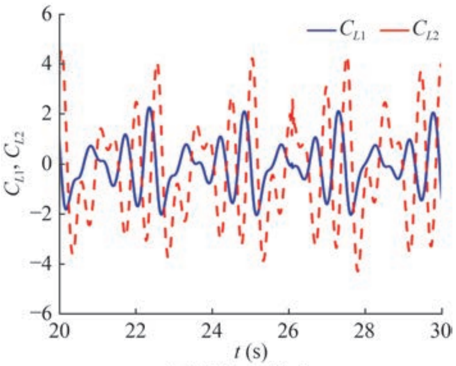

(a) Lift coefficient

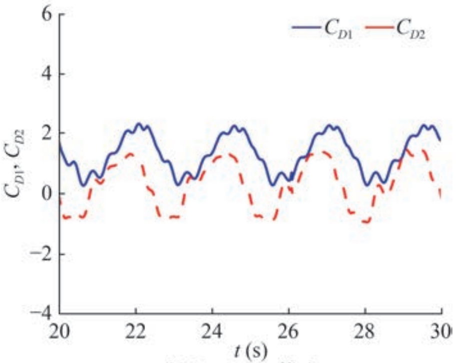

(b) Drag coefficient

Figure 17 Time histories of lift and drag coefficients at β = 45°. Solid line: upstream arm. Dashed line: downstream arm

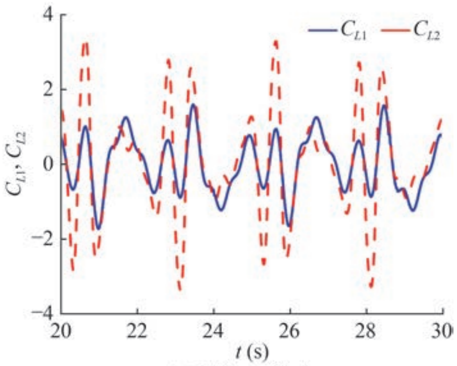

(a) Lift coefficient

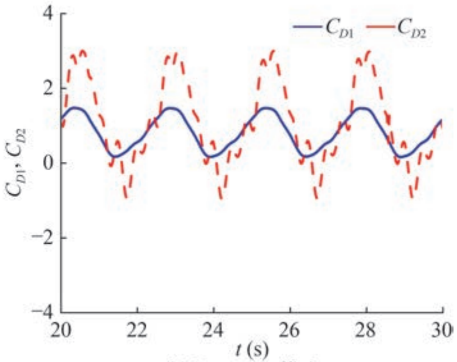

(b) Drag coefficient

Figure 18 Time histories of lift and drag coefficient at β = 315°. Solid line: upstream arm. Dashed line: downstream arm movement as the CF section changed from circular to elliptical, which aligned with the pattern shown in Figure 6. Furthermore, in contrast to Figure 16, $C_{D2,\max}$ was approximately 2.05 times greater than that of the upstream manipulator. The large spacing between the arms weakened the wake interference effect of the upstream cylinder on the downstream cylinder. Additionally, the upstream arm cross-section was elliptical; thus, the vortex generated by the upstream arm was smaller, which had a lesser influence on the stability of the downstream arm's VIV (Alam et al., 2003).

Aiming to further explore the effect of the pulsating flow on the vibration response characteristics of the different arrangements, the vortex-shedding and vibration frequencies of the underwater manipulator were analyzed for the following two arrangements: $\beta = 45°$ and 315°. Considering the existence of pulsating flow and gap fluid, the multipeak effects of vortex shedding and vibration frequency of underwater manipulators were highly evident. Figure 19 shows the spectral analysis of the vibration frequency in the manipulator and the vortex shedding frequency. As presented in Figure 19(a), in the IL direction, the vibration frequencies of each amplitude peak were generally similar, and the fundamental frequencies were 0.449 6 Hz. When $\beta = 45°$, the downstream arm vibration frequency was equal to the vortex-shedding frequency. However, the upstream arm vibration frequency differed from the vortex-shedding frequency, indicating the occurrence of beat vibration. When $\beta = 315°$, the vibration frequency in the y-direction and the vortex-shedding frequency of both arms were equal. However, the vibration frequency of the downstream arm was higher than that of the upstream arm. Simultaneously, the vibration and vortex shedding of the two arms did not achieve coordinated synchronization. In addition to the distance between the two cylinders, the upstream column shape also played an important role in influencing the VIV response (Wang et al., 2022).

Figure 20 shows the manipulator trajectory curves for two different postures. The trajectory of an object was more complex than that of a single cylinder, and the overall shape of the trajectory could not be attributed to a simple superposition of individual shapes (Wang et al., 2020).

Figures 20(a) and (b) show that the trajectories of the upstream and downstream arms were axisymmetric, which aligns with the results reported by Duan et al. (2023). When the elliptical segment was positioned upstream, the underwater manipulator maintained a relatively stable working posture. The axis of the upstream manipulator was $y_1/D = -0.01$, and its trajectory shape was similar to a "butterfly". The trajectory of the downstream arm was symmetrical, with $y_2/D = -0.05$. Comparison between Figures 21(a) and (b) showed that the displacement range of the downstream arm was larger than that of the upstream arm. By contrast, when $\beta = 315°$ (Figures 20(c) and (d)), the trajectory of the upstream arm was relatively simple, while the downstream arm exhibited a more aperiodic trajectory. The trajectory was relatively chaotic and overlapping, indicating that the downstream arm was substantially affected by interference at this time. These results further indicate that different configurations of the manipulator lead to different effects on the VIV behavior.

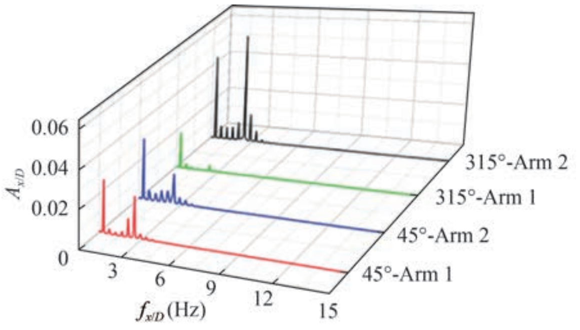

(a) In-line

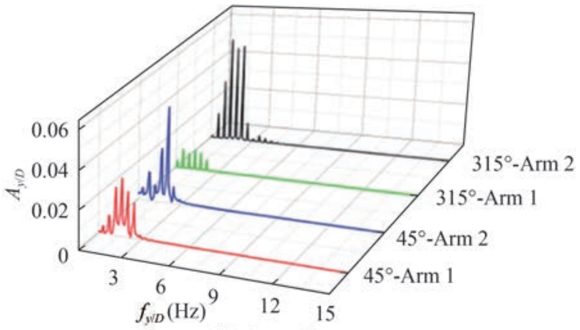

(b) Cross-flow

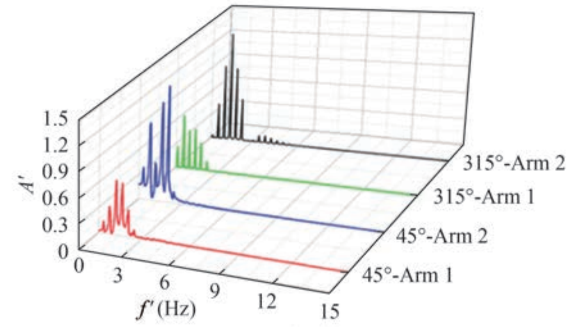

(c) Vortex shedding

Figure 19 Spectral analysis of vibration frequency and vortex shedding frequency

Figure 21 shows the vortex-shedding behavior of the manipulator with two poses over a complete cycle. When $\beta = 315°$, a stable vortex shedding was observed in the wake; when $\beta = 45°$, the wake appeared highly complex. Considerable differences were also observed in the fluid–structure coupling mechanisms of the two tandem double cylinders. As shown in Figure 21(b), when $t = t_0 + 1/4T$, the downstream arm reached its highest point. At this moment, the vortex shedding from the upstream arm collided with the lower side of the downstream arm and fused with the vortex shedding from the lower side of the down-

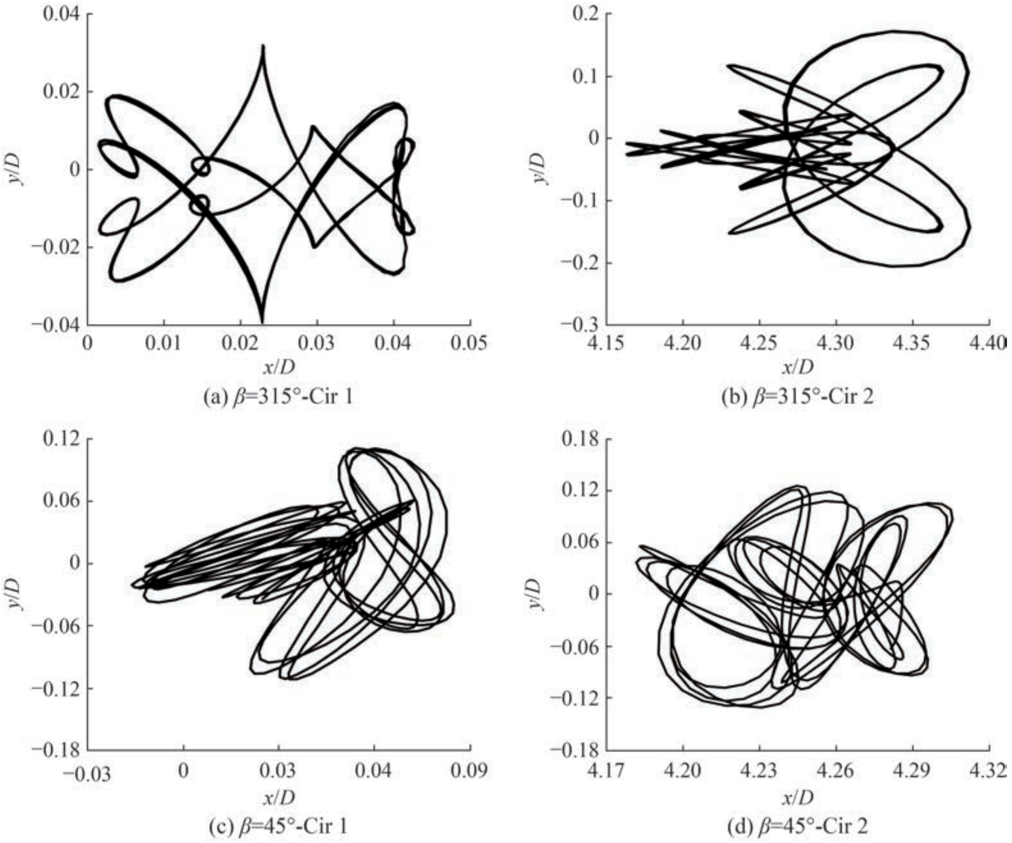

(a) β=315°-Cir 1 (b) β=315°-Cir 2

(c) β=45°-Cir 1 (d) β=45°-Cir 2

Figure 20 Trajectories of the underwater manipulator under different amplitudes

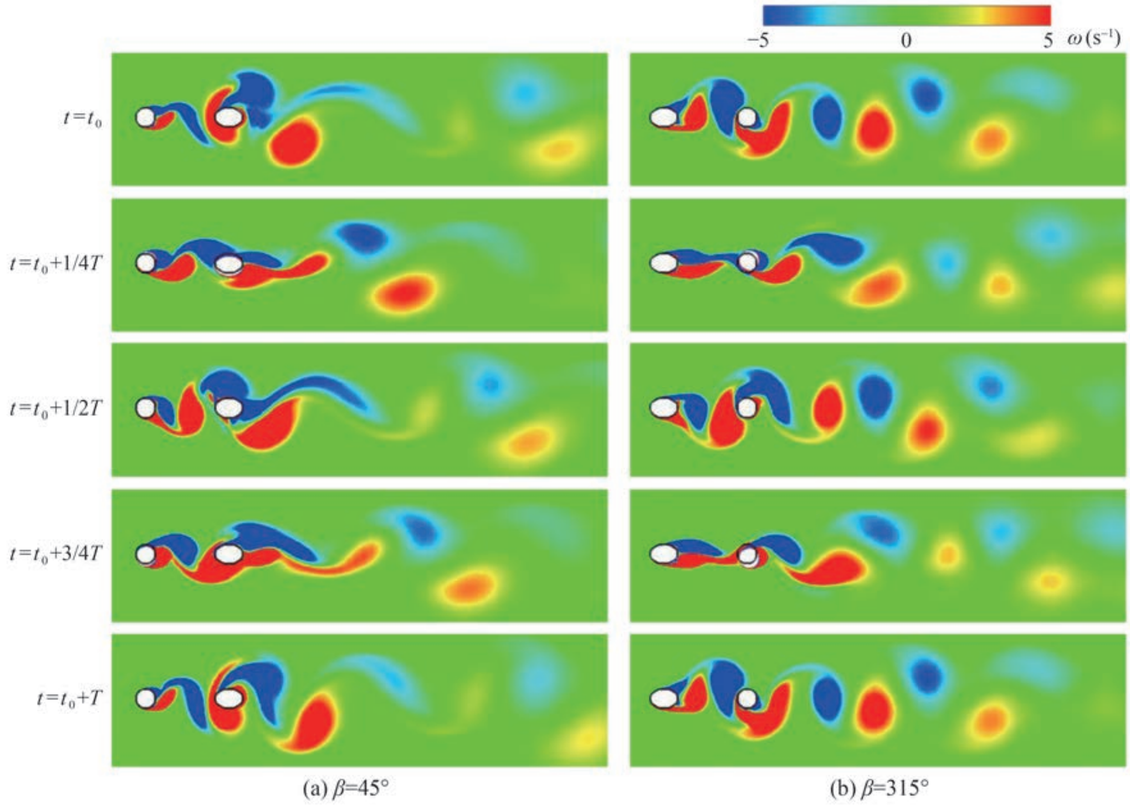

(a) β=45° (b) β=315°

Figure 21 Formation, development, and shedding of vortices in a period under pulsating flow stream arm. This interaction enhanced the vortex strength on the lower side of the downstream arm, thereby strengthening its vibration. In particular, vortex shedding with a pattern similar to the P+S pattern occurred behind the manipulator. The transverse vibration amplitude exceeded that observed in a single-arm manipulator. Compared to the VIV response of a single-arm manipulator, the motion of the downstream arm in this setup was mainly influenced by the obstruction caused by the upstream arm. This outcome was clearly different from the vortex shedding that occurred during VIV under uniform downflow conditions.

4 Conclusions

This study investigated the effects of pulsating incoming flow on the VIV response characteristics of an underwater manipulator. Aiming to better understand this behavior, the VIV response characteristics of the manipulator in different postures were compared and analyzed under pulsating and uniform flow conditions. The study also examined the effects of pulsation parameters and manipulator arrangements on the underwater manipulator's response. The key conclusions drawn from this study are presented as follows:

1) When the manipulator was in the A2 and A3 postures, $C_{L,\max}$ and $C_{D,\max}$ increased by 84.27% and 46.0%, respectively, as the incoming flow transitioned from uniform to pulsating. Moreover, the vibration trajectory of the manipulator shifted from a crescent to a sideward vase-like shape.

2) The drag coefficient and IL amplitude tended to increase as the pulsation parameter values increased. However, the lift coefficient and cross-flow amplitude increased with the pulsation frequency but decreased as the pulsation amplitude increased.

3) When the underwater manipulator was in the A1 posture, the C_L of the downstream arm increased by 99.1%, while its C_D decreased by 35.94% compared to the upstream arm. Additionally, the vibration frequency of the downstream arm in the *y*-direction was approximately 1.24 times greater than that of the upstream arm.

4) When the underwater manipulator was in the A4 posture, the C_L and C_D values of the downstream arm increased by 94.31% and 106%, respectively, compared to the upstream arm. Moreover, the vortex-shedding mode was 2P, and the motion trajectory demonstrated a regular center-symmetric profile.

The results of this study will contribute to the future exploration and utilization of marine resources. Based on the findings, the response characteristics of the underwater manipulator provide valuable insights for improving the hydrodynamic model and offer preliminary foundational research to support the stable operation of underwater manipulators in marine environments. However, considering the complexity of actual flow fields, this study simplified the analysis by assuming a stable pulsating flow field. Additionally, this study focused on a two-dimensional flow field at the middle cross-section of the manipulator to eliminate the influence of the free end on the flow field. Future research can extend this work to three-dimensional flow fields and consider factors such as the influence of the free end, cross-sectional shape, and spacing on the VIV of underwater manipulators.

Funding Supported by the National Natural Science Foundation of China (No. 51905211) and A Project of the "20 Regulations for New Universities" Funding Program of Jinan (No. 202228116).

Competing interest The authors have no competing interests to declare that are relevant to the content of this article.

References

Alam MM, Moriya M, Takai K, Sakamoto H (2003) Fluctuating fluid forces acting on two circular cylinders in a tandem arrangement at a subcritical Reynolds number. J Wind Eng Ind Aerod. 91(1-2): 139-154. https://doi.org/10.1016/S0167-6105(02)00341-0

Bao Y, Huang C, Zhou D, Tu J, Han Z (2012) Two-degree-of-freedom flow-induced vibrations on isolated and tandem cylinders with varying natural frequency ratios. J Fluid Struct. 35: 50-75. https://doi.org/10.1016/j.jfluidstructs.2012.08.002

Bourguet R, Karniadakis GE, Triantafyllou MS (2013) Phasing mechanisms between the in-line and cross-flow vortex-induced vibrations of a long tensioned beam in shear flow. Comput Struct. 122: 155-163. https://doi.org/10.1016/j.compstruc.2013. 01.002

Chen D, Marzocca P, Xiao Q, Zhan Z, Gu C (2020) Vortex-induced vibration on a low mass ratio cylinder with a nonlinear dissipative oscillator at moderate Reynolds number. J Fluid Struct. 99: 103160. https://doi.org/10.1016/j.jfluidstructs.2020.103160

Cheng Y, Duan D, Liu X, Yang X, Zhang H, Han Q (2022) Numerical study on hydrodynamic performance of underwater manipulator in the subcritical region. Ocean Eng. 262: 112214. https://doi.org/10.1016/j.oceaneng.2022.112214

Dai S, Duan D, Liu X, Jin H, Zhang H, Yang X (2025) Experimental study on vortex-induced vibration of underwater manipulator under shear flow. Journal of Marine Science and Application. https://doi.org/10.1007/s11804-025-00641-4

Dalton C, Xu Y, Owen JC (2001) The suppression of lift on a circular cylinder due to vortex shedding at moderate Reynolds numbers. J Fluid Struct. 15(3-4): 617-628. https://doi.org/10.1006/jfls.2000.0361

Duan D, Cheng Y, Liu X, Yang X, Zhang H, Han Q (2023) Study on the effect of inflow direction on the hydrodynamic characteristics of underwater manipulators. Ocean Eng. 284: 115221. https://doi.org/10.1016/j.oceaneng.2023.115221

Dalton C, Xu Y, Owen JC (2001) The suppression of lift on a circular cylinder due to vortex shedding at moderate Reynolds numbers. J Fluid Struct. 15(3-4): 617-628. https://doi.org/10.1006/jfls.2000. 0361

Deng D, Zhao W, Wan D (2021) Numerical study of vortex-induced vibration of a flexible cylinder with large aspect ratios in oscillatory flows. Ocean Eng. 238: 109730. https://doi.org/10.1016/j.

oceaneng.2021.109730

Dorogi D, Baranyi L, Konstantinidis E (2023) Modulation and hysteresis in vortex-induced vibration of a spring-mounted cylinder in a slowly varying oscillatory stream. Journal of Fluids and Structures 122: 103982

Fu B, Zou L, Wan D (2018) Numerical study of vortex-induced vibrations of a flexible cylinder in an oscillatory flow. J Fluid Struct. 77: 170-181. https://doi.org/10.1016/j.jfluidstructs.2017. 12.006

Fu S, Wang J, Baarholm R, Wu J, Larsen CM (2014) Features of vortex-induced vibration in oscillatory flow. J Offshore Mech Arct. 136(1): 011801. https://doi.org/10.1115/1.4025759

Gao Y, Zou L, Zong Z, Takagi S, Kang Y (2019) Numerical prediction of vortex-induced vibrations of a long flexible cylinder in uniform and linear shear flows using a wake oscillator model. Ocean Engineering 171: 157-171. https://doi.org/10.1016/j.oceaneng.2018.10.044

Gupta S, Patel SA, Chhabra RP (2020) Pulsatile flow of power-law fluids over a heated cylinder: Flow and heat transfer characteristics. Int J Therm Sci. 152: 106330. https://doi.org/10.1016/j.ijthermalsci.2020.106330

Jauvtis NA, Williamson CHK (2004) The effect of two degrees of freedom on vortex-induced vibration at low mass and damping. J Fluid Mech. 509: 23-62. https://doi.org/10.1017/S0022112004008778

Khalak A, Williamson CHK (1996) Dynamics of a hydroelastic cylinder with very low mass and damping. J Fluid Struct. 10(5): 455-472. https://doi.org/10.1006/jfls.1996.0031

Kim D, Song S, Jeong B, Tezdogan T, Incecik A (2021) Unsteady RANS CFD simulations of ship manoeuvrability and course keeping control under various wave height conditions. Appl Ocean Res. 117: 102940. https://doi.org/10.1016/j.apor.2021. 102940

Kozakiewicz A, Sumer BM, Fredsøe J, Hansen EA (1997) Vortex regimes around a freely vibrating cylinder in oscillatory flow. International Journal of Offshore and Polar Engineering 7: 94

Kumar D, Mittal M, Sen S (2018) Modification of response and suppression of vortex-shedding in vortex-induced vibrations of an elliptic cylinder. Int J Heat Fluid Fl. 71: 406-419. https://doi.org/10.1016/j.ijheatfluidflow.2018.05.006

Kang Z, Jia L (2013) An experiment study of a cylinder's two degree of freedom VIV trajectories. Ocean Eng. 70: 129-140. https://doi.org/10.1016/j.oceaneng.2013.05.033

Liu G, Li H, Qiu Z, Leng D, Li Z, Li W (2020) A mini review of recent progress on vortex-induced vibrations of marine risers. Ocean Eng. 195: 106704. https://doi.org/10.1016/j.oceaneng.2019. 106704

Mittal S (2017) The critical mass phenomenon in vortex-induced vibration at low. J Fluid Mech. 820: 159-186. https://doi.org/10.1017/jfm.2017.199

Muddada S, Hariharan K, Sanapala VS, Patnaik BSV (2021) Circular cylinder wakes and their control under the influence of oscillatory flows: A numerical study. J Ocean Eng Sci. 6(4): 389-399. https://doi.org/10.1016/j.joes.2021.04.002

Min XW, Chen WL, Guo YJ, Chen C (2023) Flow characteristics and mechanics of vortex-induced vibration of cable model under passive–suction–jet control. J Fluid Struct. 116: 103811. https://doi.org/10.1016/j.jfluidstructs.2022.103811

Nguyen VT, Nguyen HH (2016) Detached eddy simulations of flow induced vibrations of circular cylinders at high Reynolds numbers. J Fluid Struct. 63: 103-119. https://doi.org/10.1016/j.jfluidstructs.2016.02.004

Neshamar OE, O'Donoghue T (2022) Flow-induced vibration of a cantilevered cylinder in oscillatory flow at high KC. J Fluid Struct. 109: 103476. https://doi.org/10.1016/j. jfluidstructs.2021.103476

Qin B, Alam MM, Zhou Y (2019) Free vibrations of two tandem elastically mounted cylinders in crossflow. J Fluid Mech. 861: 349-381. https://doi.org/10.1017/jfm.2018.913

Raman SK, Arul Prakash K, Vengadesan S (2013) Effect of axis ratio on fluid flow around an elliptic cylinder—a numerical study. J Fluid Eng. 135(11): 111201. https://doi.org/10.1115/1.4024862

Raghavan K, Bernitsas MM (2008) Enhancement of high damping VIV through roughness distribution for energy harnessing at $8 \times 10^3 < Re < 1.5 \times 10^5$. Int Con Offshore Mech Arct., 871-882. https://doi.org/10.1115/OMAE2008-58006

Silva-Ortega M, Assi GRDS (2017) Suppression of the vortex-induced vibration of a circular cylinder surrounded by eight rotating wake-control cylinders. J Fluid Struct. 74: 401-412. https://doi.org/10.1016/j.jfluidstructs.2017.07.002

Sharma G, Garg H, Bhardwaj R (2022) Flow-induced vibrations of elastically-mounted C- and D-section cylinders. J Fluid Struct. 109: 103501. https://doi.org/10.1016/j.jfluidstructs.2022.103501

Shahzer MA, Khan MA, Anwer SF, Khan SA, Khan MS, Algethami AA, Alsehli M (2022) A comprehensive investigation of vortex-induced vibrations and flow-induced rotation of an elliptic cylinder. Physics of Fluids 34(3): 033605. https://doi.org/10.1063/5.0079642

Tennekes H, Lumley JL (1972) A first course in turbulence. MIT Press, Cambridge

Tu J, Zhou D, Bao Y, Ma J, Lu J, Han Z (2015) Flow-induced vibrations of two circular cylinders in tandem with shear flow at low Reynolds number. J Fluid Struct. 59: 224-251. https://doi.org/10.1016/j.jfluidstructs.2015.08.012

Williamson CHK, Govardhan R (2008) A brief review of recent results in vortex-induced vibrations. J Wind Eng Ind Aerod. 96(6-7): 713-735. https://doi.org/10.1016/j.oceaneng.2016.11.074

Williamson CH, Govardhan R (2004) Vortex-induced vibrations. Annu Rev Fluid Mech. 36: 413-455. https://doi.org/10.1146/annurev.fluid.36.050802.122128

Wang J, Zhou B, Yao Z, Yu JH, Wu Z, Zhang G (2022) The vortex-induced vibration of an elliptic cylinder with different aspect ratios. Ocean Eng. 248: 110758. https://doi.org/10.1016/j.oceaneng.2022.110758

Wang J, Fan D, Lin K (2020) A review on flow-induced vibration of offshore circular cylinders. J Hydrodyn. 32(3): 415-440. https://doi.org/10.1007/s42241-020-0032-2

Xu C, Zhang SJ, Ma J (2022) Research on cylindrical vortex induced vibration characteristics based on overset grid. Ship Sci. Technol. 44(7): 109-112. https://doi.org/10.3404/j.issn.1672-7649.2022.07.021

Yu H, Duan N, Hua H, Zhang Z (2020) Propulsion performance and unsteady forces of a pump-jet propulsor with different pre-swirl stator parameters. Appl Ocean Res. 100: 102184. https://doi.org/10.1016/j.apor.2020.102184

Yun G, Liming L, Shixiao F (2017) Study of the trajectory performance on the vortex-induced vibration response of a flexible riser. J Ship Mech. 21(5): 563-575. https://doi.org/10.3969/j.issn.1007-7294.2017.05.007

Zierenberg JR, Fujioka H, Suresh V, Bartlett RH, Hirschl RB, Grotberg JB (2006) Pulsatile flow and mass transport past a circular cylinder. Physics of Fluids 18(1): 013102. https://doi.org/10.1063/1.2164475

Zhu H, Xu B, Alam MM, Gao Y, Zhou T (2023) Vortex-induced vibration and hydrodynamic characteristics of a round-ended cylinder. Ocean Eng. 284: 115284. https://doi.org/10.1016/j.oceaneng.2023.115284

Zheng H, Wang J (2017) Numerical study of galloping oscillation of a two-dimensional circular cylinder attached with fixed fairing device. Ocean Eng. 130: 274-283. https://doi.org/10.1016/j.oceaneng.2016.11.074

Zhao M, Cheng L (2014) Two-dimensional numerical study of vortex shedding regimes of oscillatory flow past two circular cylinders in side-by-side and tandem arrangements at low Reynolds numbers. J Fluid Mech. 751: 1-37. https://doi.org/10.1017/jfm.2014.268

Zhao J, Hourigan K, Thompson MC (2019) Dynamic response of elliptical cylinders undergoing transverse flow-induced vibration. J Fluid Struct. 89: 123-131. https://doi.org/10.1016/j.jfluidstructs.2019.01.011